Investigation of the Effective Thermal Conductivity of Cell Stacks of Li-Ion Batteries

Dieter Oehler,* Jonas Bender, Philipp Seegert, and Thomas Wetzel

Knowledge of the thermal transport properties of the individual battery components and their combination is required for the design of thermally optimized lithium-ion batteries. Based on this, the limiting components can be identified and potentially improved. In this contribution, the microstructures of commercial porous electrode coatings, electrode stacks, and cell stacks are reconstructed based on experimentally determined structure parameters using a specifically developed structure generation routine. The effective thermal conductivity of the generated stacked structures is then determined by a numerical tool developed in-house based on the finite-volume method. The results are compared with an analytical model for fast accurate predictions which takes the morphological parameter sets and the geometry of the stacks into account. Both models are used to identify the system-limiting components via selected simulation studies. Finally, the results of both models are compared with experimental data for commercial electrode stacks and common literature values for cell stacks.

1. Introduction

Lithium-ion batteries (LIBs) have established themselves as the preferred storage technology in mobile applications and are regarded as the key technology for emission-free electrical automotive due to their high volumetric and gravimetric energy density and low self-discharge rate. In a LIB, a large number of unit cells are connected in parallel to provide the required electrical storage capacity. An anode stack or cathode stack consists of a current collector, which is coated on both sides with a porous mixture consisting of active material (AM) particles and the binder and carbon black (BCB) phase. A unit cell typically consists of an anode stack and a cathode stack with an electrically

D. Oehler, J. Bender, P. Seegert, Prof. T. Wetzel
Institute of Thermal Process Engineering (TVT)
Karlsruhe Institute of Technology (KIT)
Engelbert-Arnold-Str. 4, Karlsruhe 76131, Germany
E-mail: dieter.oehler@kit.edu

The ORCID identification number(s) for the author(s) of this article can be found under https://doi.org/10.1002/ente.202000722.

insulating but lithium-ion permeable porous separator in between.

However, both the operation[1] and the aging mechanisms[2–4] of LIB depend greatly on the temperature level. This originates from the temperature-dependent transport and reaction kinetics[5,6] and the electrical and thermal material properties.[7,8] The ohmic resistance of a LIB increases below 20 °C proportional to the decreasing temperature, which reduces the available power of the batteries up to 30% at 0 °C.[9,10] In addition, aging mechanisms occur at low temperatures and lead to irreversible damage to the batteries.[11–14] Lithium is separated on the anode surface, also known as lithium plating, during the charging process at low temperatures which leads to an irreversible capacity lost.[10–14] The chemical reaction rates increase exponentially above a temperature of 40 °C and undesirable side reactions occur.[10] The latter cause premature aging and a higher self-discharge rate.[10] In addition, the performance of LIB is increased for elevated temperatures. The ionic conductivity of the electrolyte increases and causes a decrease in the ohmic resistance.[15] Furthermore, the diffusion overvoltage is reduced due to the faster diffusion transport processes at higher temperatures.[15] As a result, an operating window of 20–40 °C is recommended to ensure efficient use and reduced aging mechanisms.[10]

Heat dissipation occurs inside a LIB as a result of ohmic resistances and electrochemical reactions during operation,[5] which leads to elevated battery temperatures under high electrical loads. Schuster et al.,[16] Ramadass et al.,[17,18] Zhang et al.,[19] and Fleckstein et al.[20] confirm the dependence of the aging mechanisms at elevated temperature levels mentioned earlier. Furthermore, the authors show that the aging mechanisms also depend on nonuniform temperature distributions caused by thermal management systems. Therefore, well-designed thermal management systems are required to avoid adverse or even critical thermal conditions inside a LIB. Hence, the knowledge of the electrochemical–thermal behavior of the batteries is indispensable.

Numerous authors, such as Guo et al.,[21] Jeon et al.,[22] and Yue et al.,[23] have developed electrochemical–thermal models to predict the complex spatial nonuniformity battery temperature as a function of the homogenization degree of their thermal models. Hence, the models of the authors mentioned depend on the exact knowledge of the thermal transport properties of the individual cell layers, consisting of anodes, cathodes, and

**ADVANCED
SCIENCE NEWS**

www.advancedsciencenews.com

Energy Technology
Generation, Conversion, Storage, Distribution

www.entechnol.de

separators. Chen et al.,[24] Samba et al.,[25,26] and Goutam et al.[27] homogenize the inner cell layers in their thermal models and need, therefore, homogeneous thermal transport properties for the inner cell core (jelly roll or stack).

According to the contributions of Maleki et al.,[7] Richter et al.,[28] Loges et al.,[29] and Chen et al.,[30] the effective thermal conductivity of porous anodes varies between 0.26 and $3.5 \, \text{W m}^{-1} \, \text{K}^{-1}$, depending on the measuring method and fluid within the pore spaces during measurement. Gases, such as helium, nitrogen, and carbon dioxide, are used as filling fluids for the pore space instead of the extremely volatile electrolytes caused by their incompatibility with established measurement methods. The authors mentioned reported values between $0.13–2.49 \, \text{W m}^{-1} \, \text{K}^{-1}$ for the effective thermal conductivity of porous cathodes, depending on the AM and filling fluid. Richter et al.[28] determined experimental effective thermal conductivity values of $0.1–0.4 \, \text{W m}^{-1} \, \text{K}^{-1}$ for electrolyte-soaked separators. Drake et al.,[31] Murashko et al.,[32] Bazinski and Wang,[33] Sheng et al.,[34] Zhang et al.,[35] and Maleki et al.[36] report effective thermal conductivity values for entire LIB and homogeneously resolved inner cell cores perpendicular to the cell layer direction (through-plane) between $0.15–1.63 \, \text{W m}^{-1} \, \text{K}^{-1}$.

The wide ranges, unknown structural parameters, and low number of values from only a few publications make identifying representative effective thermal conductivity values for the individual cell layers difficult. The experimental determination of these values is time-consuming, expensive and associated with high uncertainties. In this regard, we present in this work a new modeling concept for the determination of the effective thermal conductivity of porous anode stacks, cathode stacks and separators, and homogeneous cell stacks. Therefore, our analytical and numerical model approaches[37] for porous electrode coatings presented previously, which consider a large set of microstructural parameters and the thermal bulk material properties, have been extended to electrode and cell stacks. The analytical model is a precise and fast model, representing the various complex thermal transport paths within the porous electrode coatings. The particle contact areas, the particle distances, the BCB phase, and its distribution by combinations of weighted parallel and series connections are also considered. By contrast, the numerical model is based on a 3D generic geometry generation of the porous electrode structures and their solution of the heat conduction equation using the finite-volume method. The models are verified against each other and validated by experimentally determined effective thermal conductivities of the electrode stacks of two disassembled commercial high-power cells originating from the manufacturer KOKAM. The microstructure parameters, such as the geometric dimensions, volume fractions of the AM particles, the BCB phase, and the pore space, as well as the particle size distributions of the electrode stacks of the cells mentioned are taken from focused-ion beam–scanning electron microscopy (FIB–SEM) images.[38] In a next step, the electrode stacks are reconstructed under the use of the extended structure generation routine. The effective thermal conductivity of separator layers is estimated by established analytical models for binary component systems for the calculation of the effective thermal conductivity of entire cell stacks. The cell stacks of the KOKAM cells are then reconstructed by the structure generation

routine and the effective thermal conductivity of the stacks is determined numerically as a function of the estimated thermal conductivity boundaries of the separator layers mentioned earlier. Again, the values are compared with the analytical model and validated by experimental literature data.

The thermal conductivity of the individual cell layers can differ by several orders of magnitude, which results in an anisotropic behavior of the effective thermal conductivity perpendicular or parallel to the stacking direction. This article initially deals with the effective thermal conductivity perpendicular to the stacking direction of anode and cathode stacks. Afterward, the anode stacks, cathode stacks, and separators are combined to cell stacks to determine the effective thermal conductivity perpendicular as well as parallel to the layer direction.

The article is organized in the following manner: The structure generation routine is briefly repeated in Section 2.1. Section 2.2 deals with the extension of the structure generation routine by separator and current collector layers or further electrode coatings to electrode and cell stacks. In Section 2.3, the definition of the effective thermal conductivity is introduced and adapted to electrode and cell stacks. Section 3.1 and 3.2 explain the analytical model based on thermal resistance networks, developed previously for porous electrode coatings, and its extension to electrode and cell stacks. Section 3.3 presents classic analytical modeling approaches for heterogeneous binary component systems and their application to porous separators. In Section 4, the reconstructed porous electrode coatings, electrode stacks, and cell stacks for the investigated cells are discussed. Using the reconstructed structures, numerous simulation studies for the electrode coatings, electrode stacks, and cell stacks are conducted. The results of the models are also compared with our own experimental measurements and existing literature data to check their validity. Section 5 provides a summary.

2. Numerical Simulation

2.1. Microstructure Generation

In our previous publication,[37] we presented a generic geometry generation routine for porous electrode coatings. In this work, the structure generation routine developed is extended by current collectors and separator layers so that the effective thermal conductivity of electrode stacks and cell stacks can be determined. Therefore, we will briefly explain the functionality of the routine. The input parameters of the routine represent the particle size distribution, the particle shape, the initial rotation, the volume fractions of the AM particles, and the homogeneous BCB phase as well as the type of BCB distribution. In a first step, particles are dropped as graphic objects stochastically into a cuboidal system volume of predefined size, one after another, and sedimented until a stable position of each particle is reached. A stable position is reached if the particle crosses the lower system limitations or a collision with an already sedimented particle occurs where no further lowering of the particle is possible (**Figure 1**). The collision detection is carried out by the Gilbert–Johnson–Keerthi algorithm.[39] The lower system boundary is called the current collector cut (according to Figure 1), where the contact area between the current collector and the particles in the
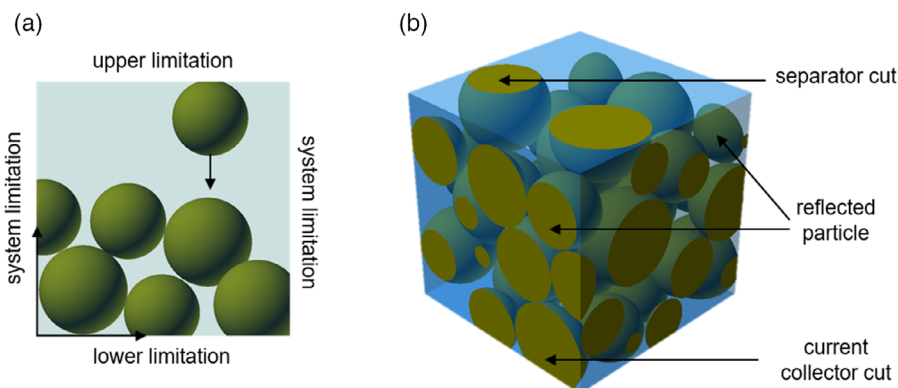
Figure 1. a) Illustration of the system limitations and the sedimentation process. b) Representation of the system volume, the current collector cut, and the separator cut. Reproduced with permission.[37] Copyright 2020, Wiley.

sedimentation process can be adjusted. The upper system boundary is called the separator cut (according to Figure 1) and analogous to the current collector cut, the contact area between the particles and separator can be adjusted.

In the next step, the information of the porous particle structure generated, such as the Cartesian coordinates of the particle centers and the size and shape of the particles, are automatically transferred to OpenSCAD, a code-based open source computer-aided design (CAD) program. The information is stored as string variables in form of SCAD files for each individual particle. In a final step, the BCB phase considered homogeneously is created in the form of binder shells and/or bridges. The geometric information of the individual binder shells or bridges is again stored as string variables in SCAD files. After a check of the geometry, all SCAD files of the individual phases are converted into stereolithography (STL) files, which are needed for the numerical simulation tool. **Figure 2**a shows a particle covered by a binder shell, Figure 2b a binder bridge between two particles, and Figure 2c a mixed particle structure with binder shells and bridges.

2.2. Generation of Electrode Stacks and Cell Stacks

In the following section, the extension of the electrode coatings by current collector and separator layers to electrode stacks and cell stacks is discussed. First, the structure of electrode stacks and cell stacks is briefly explained according to the schematic shown
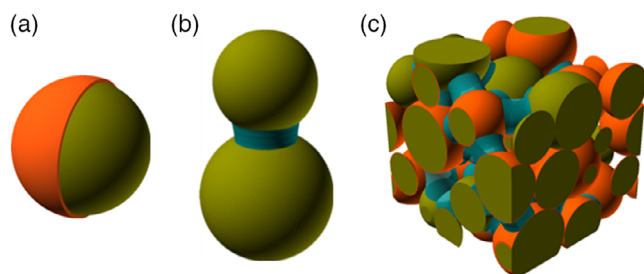
Figure 2. Representation of a) a particle covered by a binder shell, b) a binder bridge between two particles, and c) a mixed particle structure with binder shells and bridges.
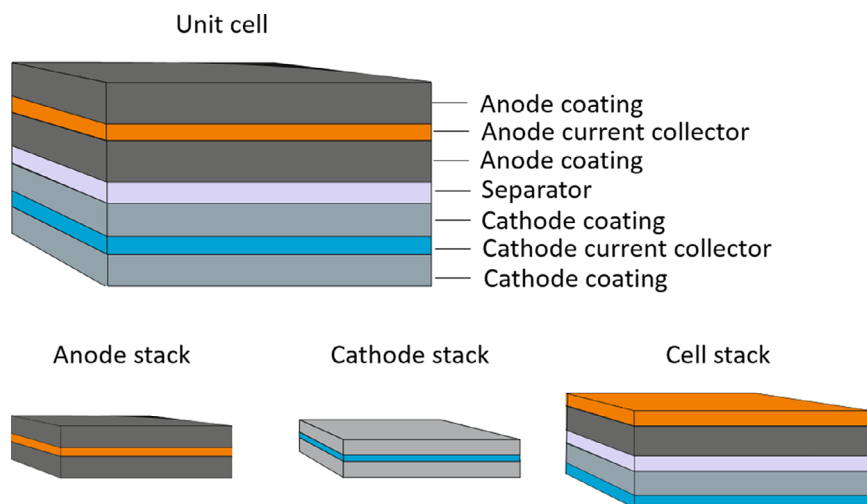
in **Figure 3**. In this contribution, a unit cell of a LIB cell consists of two electrode stacks which are separated by an electrically isolating, lithium-ion permeable separator. An electrode stack (anode stack or cathode stack) consists of a current collector, which is coated on both sides with a porous mixture consisting of AM particles and the BCB phase. The pore space of the porous electrode coating is filled with an electrolyte. A cell stack consists of half the anode current collector, a single-sided anode coating, the separator, a single-sided cathode coating, and half the cathode collector. The pore space between the coating and separator is again filled with electrolyte.

Electrode coatings can be automatically extended to electrode and cell stacks using the CAD tool OpenSCAD. Individually designed layer composites can be generated based on user-defined specifications, such as layer thickness and the type of layer. **Figure 4** shows an example of a porous coating that has been extended by a current collector and/or separator. After the generation of the layer composites, SCAD files are automatically created for the new layers and then converted into STL files.

The postprocessing phase is initiated after the completion of the structure generation. The STL files of the particles, binder shells and/or bridges, current collectors, and separators are automatically transferred to the meshing tool snappyHexMesh for the creation of the discretization grid. All grid cells of the porous coating that do not belong to the AM or BCB phase are assigned to the electrolyte.

2.3. Numerical Determination of the Effective Thermal Conductivity

Heterogeneous material systems, such as porous electrode coatings, electrode stacks, and cell stacks, are regarded as black boxes. Therefore, the concept of the effective thermal conductivity is used. As reported in our previous publication,[37] the effective thermal conductivity of porous electrode coatings or layered composites can be calculated by applying a temperature gradient. The latter induces a heat flow which, according to the second law of thermodynamics, flows from a higher to a lower temperature.[40] The Fourier heat conduction equation can be applied in the case of 1D and stationary heat conduction.[40] Hereby, $\dot{Q}$ represents the heat flow, λ_{eff} is the effective thermal conductivity, A is the

ADVANCED
SCIENCE NEWS
www.advancedsciencenews.com

Energy Technology
Generation, Conversion, Storage, Distribution
www.entechnol.de

Figure 3. Illustration of a unit cell, an anode stack, a cathode stack, and a cell stack of a lithium-ion battery.
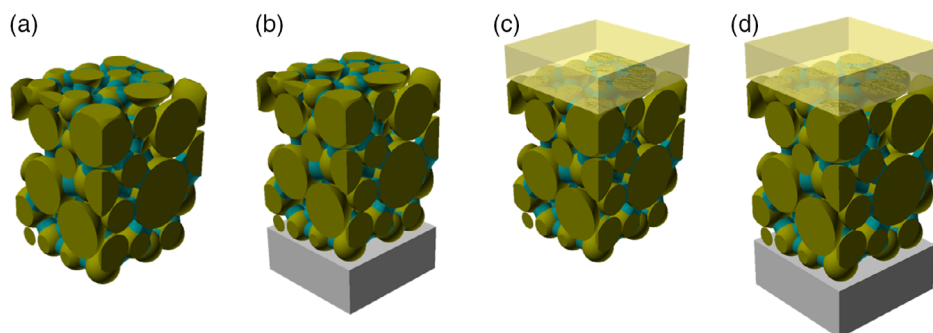

Figure 4. a) Electrode coating, b) with current collector, c) with separator, and d) with current collector and separator.

cross-sectional area, and T_1 and T_2 are the adjacent temperatures, see Equation (1).

$$\dot{Q} = -\lambda \cdot A \cdot \frac{dT}{dx} = -\frac{\lambda_{\text{eff}}}{s} \cdot A \cdot (T_2 - T_1) \tag{1}$$

Figure 5a shows an example of a cell stack with an applied temperature gradient perpendicular to the cell layers. This corresponds to a first-order boundary condition, also called a
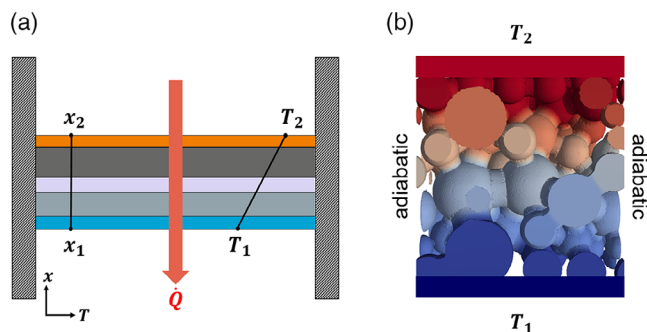
Figure 5. a) Schematic representation of a cell stack as a black box system. b) Illustration of the temperature profile of a porous electrode coating using the Neumann and Dirichlet boundary conditions.

Dirichlet condition ("fixed value"). The shaded system boundaries are considered adiabatic, therefore, a second-order boundary condition according to Neumann ("zero gradient") is applied. A porous electrode coating is shown in Figure 5b as an example in which the resulting temperature profile can be seen using the boundary conditions mentioned earlier. Within the scope of this publication, the resulting heat flow through a specified geometry is determined by a numerical thermal simulation by applying a temperature gradient and defined boundary conditions. As a result, the effective thermal conductivity can be determined according to Equation (2).

$$\lambda_{\text{eff}} = \frac{\dot{Q} \cdot s}{A \cdot (T_1 - T_2)} \tag{2}$$

The open source software package OpenFOAM, which is based on the finite-volume method, is used for the solution of the steady-state heat conduction problem and for determination of the heat flow $\dot{Q}$. The numerical solution method was explained in detail in our previous work[37] and is, therefore, not the subject of this article. After the completion of the numerical simulation, the postprocessing tool wallHeatFlux from OpenFOAM is used to calculate the incoming and outgoing heat flow through each individual region (particle, binder shells, binder bridges,

electrolyte, current collector, and separator). The thermal conductivity results from Equation (2) considering the mean heat flow of the hot (top) and cold (bottom) side (according to Figure 5a).

3. Analytical Model

3.1. Porous Electrode Coating

An analytical model for the determination of the effective thermal conductivity of porous electrode coatings (reported previously[37]) is briefly explained in the following section and extended to electrode and cell stacks. The approach is based on the well-known Zehner, Bauer, and Schluender (ZBS) model,[41–43] which was originally developed for classic porous particle beds. The idea of the modeling approach is the description of the effective thermal conductivity of porous structures using thermal resistance networks. The networks consist of a combination of series and parallel connections of thermal resistors. **Figure 6**b shows the extension of the ZBS model for porous electrode coatings. The bulk thermal conductivities and volume fractions of the AM phase λ_{AM}, ν_{AM}, the BCB mixture λ_{BCB}, ν_{BCB}, and the fluid phase λ_F, ϕ, as well as the particle distance factor c and the particle contact area parameter α are the input parameters of the analytical model, as shown in Equation (3).

$$\lambda_{eff} = f(\lambda_{AM}, \lambda_{BCB}, \lambda_F, \nu_{AM}, \nu_{BCB}, \phi, c, \alpha) \tag{3}$$

In Figure 6a, the three main heat conduction pathways of porous electrode coatings are shown schematically. Pathway 1 describes the heat conduction through the fluid/electrolyte phase and pathway 2 through the AM phase, caused by contact areas of the AM particles. By contrast, pathway 3 represents a mixture of the fluid, AM, and the homogeneously considered BCB phase. A rotationally symmetric section of the thermal resistance network of the extended ZBS model is shown in Figure 6b. The network is

based on the assumption that the three main heat conduction paths are connected in parallel. Hereby, the main heat conduction paths are weighted according to system-specific microstructure parameters. The derivation of the resistance network and the explanation of the weighting parameters of the main heat conduction pathways can be found in our previous publication.[37]

3.2. Electrode Stacks and Cell Stacks

The model mentioned earlier can be extended by further layers connected in series or parallel for the calculation of the effective thermal conductivity of entire electrode and cell stacks. Additional layers can correspond to further porous electrode coatings, current collectors, or separators. The effective thermal conductivity perpendicular to the stacking direction can be described by the series connection of thermal resistors, according to Equation (4).

$$\lambda_{eff,\perp} = \frac{L_{ges}}{\sum_{i=1}^{n} \frac{L_{layer,i}}{\lambda_{layer,i}}} \tag{4}$$

The effective thermal conductivity parallel to the layers can be described by the parallel connection of thermal resistors, according to Equation (5).

$$\lambda_{eff,\parallel} = \frac{\sum_{i=1}^{n} L_{layer,i} \cdot \lambda_{layer,i}}{L_{ges}} \tag{5}$$

3.3. Porous Separator

Different modeling concepts for estimating minimal and maximal values of the effective thermal conductivity of porous separators are presented in the following section. Separators are porous multiphase structures which include a complex network of interconnected and irregular pores or channels.[44,45]
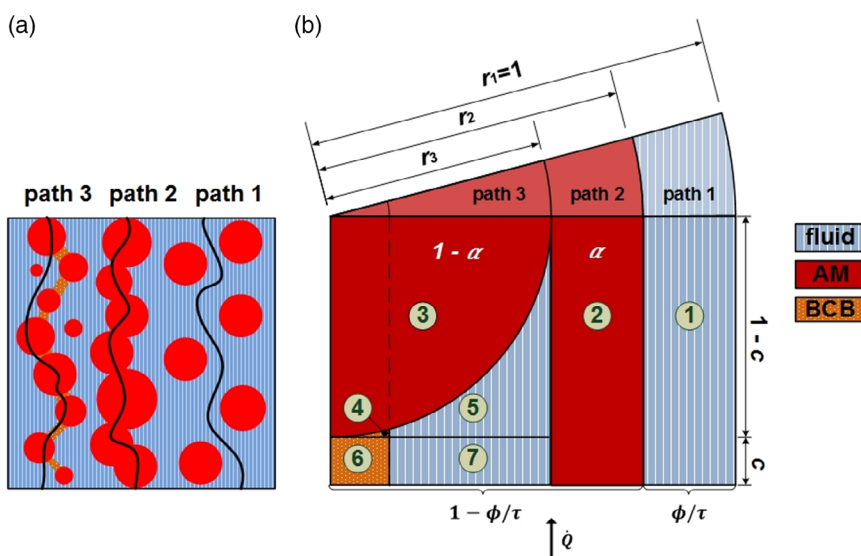
Figure 6. a) Illustration of the three main heat conduction paths in porous electrode coatings. b) Illustration of the thermal resistance network of the extended ZBS model for porous electrode coatings. Reproduced with permission.[37] Copyright 2020, Wiley.

Commercially available LIB separators typically consist of polymers, such as polyethylene and polypropylene.[44,45] Separators can be regarded as a binary component system consisting of the polymer matrix and the fluid/electrolyte in the pore spaces. The volume fraction and thermal conductivity of the polymer is abbreviated to ν_{PM}, λ_{PM} and that of the fluid to ν_F, λ_F. The parallel connection can be used to determine the upper limit of the effective thermal conductivity of the porous separator. By contrast, the series connection represents the lower limit of the effective thermal conductivity. The Maxwell–Eucken bounds are the narrowest possible limits for macroscopically homogeneous, isotropic, two-phase materials.[46–48] The limits of the Maxwell–Eucken models always lie within the series and parallel connection bounds, independent of the components volume fraction and thermal conductivities.[46–48] The fluid is considered as continuous and the polymer as dispersed phase in the Maxwell–Eucken model I. In the Maxwell–Eucken model II, the polymer is considered as continuous and the fluid as dispersed phase. Both components are considered randomly distributed in the effective medium theory (EMT), i.e., none of the phases is continuous or disperse.[48–50] Each of the two components can form continuous heat conduction pathways, which depend on the volume fraction of the respective phases. **Table 1** shows the models
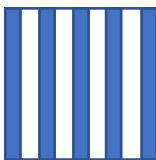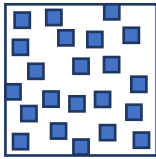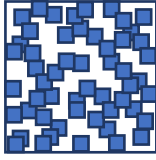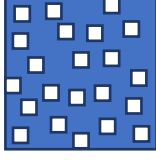
mentioned earlier, their structure and their equations for the calculation of the effective thermal conductivity.

4. Results and Discussion

### 4.1. Generic Reconstruction of Two Lithium-Ion Cells

This section deals with the reconstruction of porous electrode coatings, electrode stacks, and cell stacks of two commercial high-power cells manufactured by KOKAM. Therefore, the structure generation routine, presented previously in Section 2, is used. Necessary experimentally determined morphological parameters of both cells were required to ensure a realistic reconstruction of the geometry. Known morphological parameter sets of the cells are taken from the study by Almar et al.[38] and unknown parameter sets are determined experimentally within the scope of this work. First, we will briefly discuss the morphology of typical porous electrode coatings. The porous electrode coating consists of a fluid and a solid phase. The fluid phase is an electrolyte which is located in the pore spaces of the porous coatings. The solid phase of the porous coatings is regarded as a heterogeneous material system consisting of AM particles and a BCB mixture. The AM particles of both the anode and cathode

Table 1. Illustration of different models for the estimation of the minimal and maximal bounds for the effective thermal conductivity of heterogeneous two-component systems.

Model	Structure	Effective thermal conductivity equation	Ref.
Parallel connection		$\lambda_{eff} = \nu_F \cdot \lambda_F + \nu_{PM} \cdot \lambda_{PM}$	–
Maxwell–Eucken I ν_F continuous phase ν_{PM} disperse phase		$\lambda_{eff} = \dfrac{\nu_F \cdot \lambda_F + \nu_{PM} \cdot \lambda_{PM} \cdot \frac{3 \cdot \lambda_F}{2 \cdot \lambda_F + \lambda_{PM}}}{\nu_F + \nu_{PM} \cdot \frac{3 \cdot \lambda_F}{2 \cdot \lambda_F + \lambda_{PM}}}$	[46,47]
EMT model		$\nu_F \cdot \dfrac{\lambda_F - \lambda_{eff}}{\lambda_F + 2 \cdot \lambda_{eff}} + \nu_{PM} \cdot \dfrac{\lambda_{PM} - \lambda_{eff}}{\lambda_{PM} + 2 \cdot \lambda_{eff}} = 0$	[49,50]
Maxwell–Eucken II ν_{PM} continuous phase ν_F disperse phase		$\lambda_{eff} = \dfrac{\nu_{PM} \cdot \lambda_{PM} + \nu_F \cdot \lambda_F \cdot \frac{3 \cdot \lambda_{PM}}{2 \cdot \lambda_{PM} + \lambda_F}}{\nu_{PM} + \nu_F \cdot \frac{3 \cdot \lambda_{PM}}{2 \cdot \lambda_{PM} + \lambda_F}}$	[46,47]
Series connection		$\lambda_{eff} = \dfrac{1}{\nu_F / \lambda_F + \nu_{PM} / \lambda_{PM}}$	–

coatings can be regarded as spheres, as shown in the SEM images in previous studies.[51–53] Indrikova et al.[54] investigated the distribution of the BCB phase within different porous electrode coatings. They showed that the amount of the BCB phase that coats the AM particles homogeneously is negligible compared with the amount of the BCB that forms bridge-like structures between the AM particles. This conclusion is also confirmed by different SEM images of BCB distributions of the publications from Bauer et al., Pfaffmann et al., and Wang et al.[55–57]

Bearing in mind the publications mentioned earlier, the BCB phase is realized in the form of homogeneous binder bridges in the generic reconstructions of the porous electrode coatings of the two commercial KOKAM cells. **Figure 7** shows an example of the generation process of a generic binder bridge between two AM particles. The generation of a binder bridge can be divided into three consecutive steps: a) The BCB phase is generated by extruding a polygon to a rotational body, b) the rotational body is
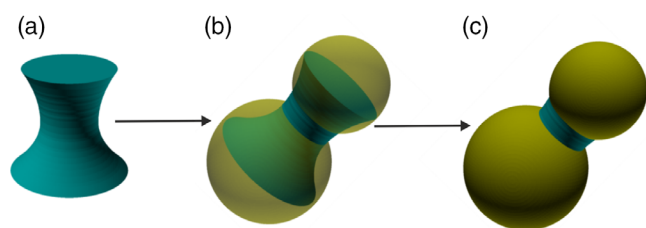
Figure 7. Illustration of the stepwise generation of a binder bridge: a) extruding a polygon to a rotational body, b) positioning of the body between two AM particles, and c) intersection of the polygon and the AM particles.

positioned between two AM particles, and finally, c) the binder bridge results from the intersection of the rotational body and the AM particle. The average surface coverage of the active particles by the BCB mixture is about 35–40% in the case of binder bridges, which corresponds to the literature value of 40% according to Yoo et al.[58]

Two commercial high-power cells manufactured by KOKAM at begin of life with a capacity of 350 mAh (cell A) and 3.2 Ah (cell B) in a discharged state (implies a State of Charge 0%) are regarded in the following. **Table 2** shows the specifications of the two KOKAM cells A and B. The geometry and morphological parameters of the reconstructed individual cell layers are shown in **Table 3**.

As the composition of the separator is not known in detail, a variation of the separator thermal conductivity is carried out in Section 4.3 to estimate the sensitivity to the effective thermal conductivity of the cell stack.

First, the morphological parameter sets of both KOKAM cells required for the generic reconstruction of the electrode coatings, electrode stacks, and cell stacks are discussed. The volume fractions of the AM phase, the BCB phase, the particle size distribution of the AM and the geometry of the particles, as well as the thicknesses of the individual layers must be defined as input parameters for the structure generation routine for the reconstruction of commercial electrode coatings, electrode stacks, and cell stacks on a one-to-one scale. In a next step, the parameter sets of the cathode coatings will be discussed. The porosities of the cathode coatings were determined via mercury porosimetry. Values of 32.4 vol% for cell A and 30 vol% for cell B for the cathode coatings result. Identical high-power cells of the manufacturer KOKAM were investigated regarding their BCB fraction in the publication of Almar et al.[38] Based on FIB–SEM images,

Table 2. Specifications of the high-power KOKAM SLPB 283452H (cell A) and KOKAM SLPB 8043140H5 (cell B).

Cell properties	KOKAM SLPB 283452H (cell A)	KOKAM SLPB 8043140H5 (cell B)
Cell type	High-power cell	High-power cell
Cell capacity	350 mAh	3.2 Ah
Voltage range	2.7–4.2 V	2.7–4.2 V
Cell chemistry	Graphite—LCO/NCA[59–61]	Graphite—LCO/NCA[3,4]
Separator	Polyethylene/polypropylene[a]	Polyethylene/polypropylene[a]
Electrolyte	LP30[a] (1.0 M LiPF6; dimethylcarbonat (DMC)/ethylencarbonat (EC) = 50/50 wt%/wt%)	LP30[a] (1.0 M LiPF6; DMC/EC = 50/50 wt%/wt%)

[a]Estimated.

Table 3. Morphological parameters and layer thicknesses of the reconstructed electrode coatings, electrode stacks, and cell stacks of cell A and cell B.

Structural parameters	Cathode coating [c, pos]		Cathode current collector [cc, pos]		Anode coating [c, neg]		Anode current collector [cc, neg]		Separator [sep]	
	Cell A	Cell B	Cell A	Cell B	Cell A	Cell B	Cell A	Cell B	Cell A	Cell B
Thickness L_i [μm]	25	27.5	27	25	45	42	20	25	17	18
Porosity [vol%]	32.5	30.9	–	–	26.3	26.7	–	–	–	–
BCB fraction [vol%]	12.7	12.9	–	–	18.5	18	–	–	–	–
AM fraction [vol%]	54.8	56.2	–	–	55.2	55.3	–	–	–	–
Sauter mean diameter [μm]	5.3		–	–	8.9		–	–	–	–

**ADVANCED
SCIENCE NEWS**

www.advancedsciencenews.com

Energy Technology
Generation, Conversion, Storage, Distribution

www.entechnol.de

they determined average values of 12.7 vol% for the BCB phase of the cathode coatings. Regarding the generic reconstruction of the BCB phase, the average value determined by Almar et al.[38] is defined as the input value for both the KOKAM cells A and B. The volume fractions mentioned earlier result in a value for the cathode AM phase for cell A of 55 vol% and for cell B of 56 vol%. The particle size distributions of the porous cathodes of the high-power KOKAM cells were also examined in the contribution of Almar et al.[38] Therefore, these particle size distributions, determined with a mean Sauter diameter of 5.3 μm, are used as input parameters for the reconstruction of both the cathode coatings. The thicknesses of the cathode coatings of cell A at 25 μm and cell B at 27.5 μm were determined experimentally using microscope images and a micrometer screw.

The porosities of the anode coatings were also experimentally determined via mercury porosimetry. Values of 26.8 vol% for cell A and 27.4 vol% for cell B were measured for the anode coatings. Based on FIB–SEM images, a BCB fraction of 17.9% was determined for both the anode coatings of the KOKAM cells. Furthermore, the particle size distribution of the anode AM with an average Sauter diameter of 8.9 μm was extracted from the images. The volume fractions mentioned earlier result in a value of 55 vol% for the cathode AM phase for both cell A and cell B. The thicknesses of the anode coatings were determined analogous to that of the cathode coatings using microscope images and a micrometer screw. Values of 45 μm for cell A and 42 μm for cell B were measured for the anode coating.

The morphological parameters of the reconstructed electrode coatings of cell A and cell B mentioned earlier are shown in Table 3. Structures with cross-sectional dimensions of $15 \times 15 \, \mu m^2$ are generated, which corresponds to 5–6 million grid cells. This is caused by the fact that system volumes of larger dimensions do not show significant changes in the effective thermal conductivity. **Figure 8**a shows the generically reconstructed cathode coatings and Figure 8b the generically reconstructed anode coatings of cell A and cell B. In addition, the target volume fractions of all phases were reproduced with a mean deviation of less than 1 vol%. Furthermore, the complex pore structures of the commercial electrode coatings were approximated considering the possibility of overlapping binder bridges to reconstruct a realistic BCB network. Therefore, the

distribution shown in Figure 8 can be compared by the SEM images in the publications.[55–57]
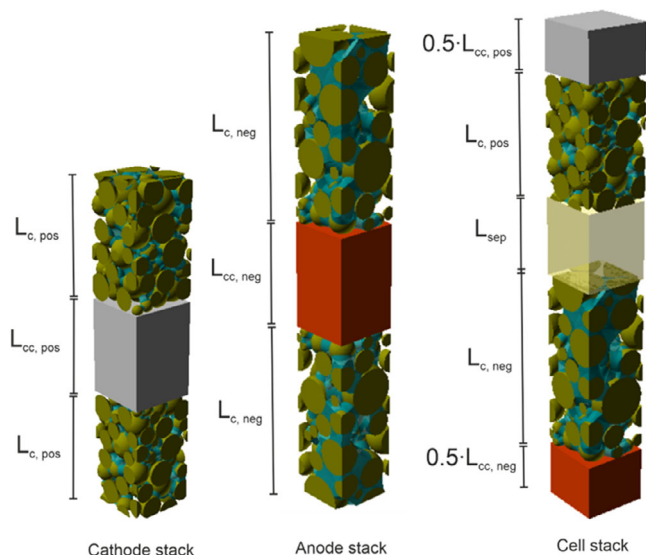
The extended structure generation routine presented in Section 2.2 is used for a true-to-scale reconstruction of the electrode stacks and cell stacks. The thicknesses of the cathode current conductor of cell A at 25 μm and cell B at 27 μm were determined experimentally using microscope images and a micrometer screw. Values for the anode current collector of 20 μm for cell A and 25 μm for cell B were measured. In addition, values for the thicknesses of the separators for cell A of 17 μm and for cell B of 18 μm have been determined also with microscope images and a micrometer screw. The results agree very well with Mayur et al.[61] who measured a thickness of 16 μm for the separator of the cell A. The mean deviations of the layer thicknesses for the microscope images compared with the micrometer screw are about 2 μm. Therefore, we have used the mean value of the two measuring methods. Only half the thicknesses of the current collectors are considered for a representative cell stack, as described in Section 2.2.

The separator is considered as a homogeneous layer in the numerical reconstructions. The assumption of a homogeneous separator layer represents a simplified, but precise description of its effective thermal conductivity, with the benefit of an efficient reduction of computing time. In addition, the thermal conductivity of the solid polymer matrix (e.g., polyethylene and polypropylene)[62–64] and the liquid electrolyte (e.g., LP30)[65] is very close to each other, so that local microstructural influences such as differences in porosity and tortuosity only play a minor role. Therefore, the analytically heterogeneous modeling approaches presented in Section 3.3 approximate the effective thermal conductivity very accurately. As input parameter for the effective thermal conductivity of the homogeneous separator in the numerical model, the results of the analytical modeling approaches depending on the porosity and bulk thermal conductivities of the separator materials are used. **Figure 9** shows examples of reconstructed electrode stacks and cell stacks; the corresponding dimensions of the layer thicknesses for cell A and cell B are shown in Table 3. Structures with cross-sectional dimensions of $15 \times 15 \, \mu m^2$ are generated, which have 8–10 million grid cells.
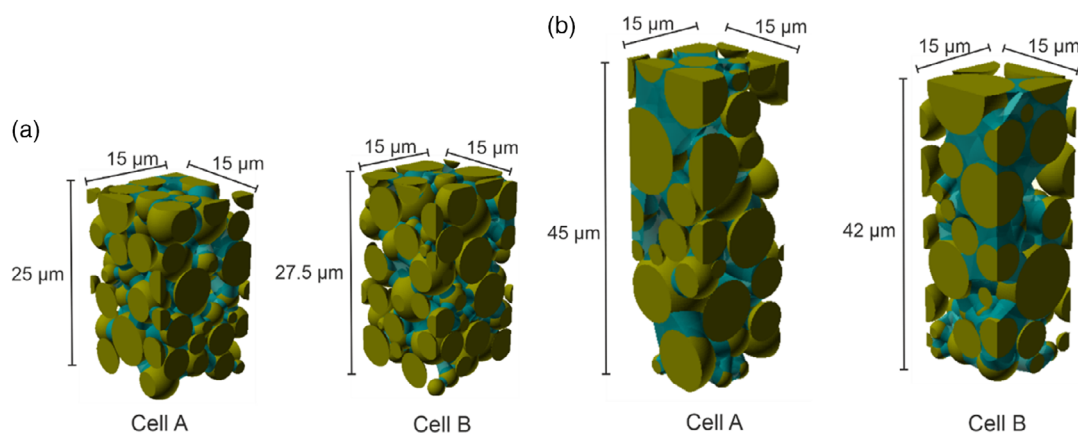
Figure 8. Representation of the generically reconstructed electrode coatings of cells A and B: a) cathode coating and b) anode coating.

**ADVANCED
SCIENCE NEWS**

www.advancedsciencenews.com

Energy Technology

Generation, Conversion, Storage, Distribution

www.entechnol.de

Figure 9. Exemplary representation of a cathode stack, anode stack, and cell stack.

4.2. Thermal Transport Properties

In addition to the morphological parameter sets, an exact knowledge of the thermal transport properties of the individual bulk materials is necessary for a precise modeling of the effective thermal conductivity. For this purpose, an extensive literature study focusing on the thermal conductivity of the bulk materials was carried out. The results of the study refer to an average temperature of about 25 °C and the corresponding values are shown in **Table 4**. The usual cathode AM is lithium-cobalt-oxide (LCO) or lithium-nickel-manganese-cobalt-oxide (NMC). An average thermal conductivity of 3.5 W m^{-1} K^{-1}[66–71] was found for polycrystalline LCO, with a typical grain size of 2 nm. Cheng et al.[72] determined a thermal conductivity of 4.2 W m^{-1} K^{-1} for NMC, which deviates only by 0.7 W m^{-1} K^{-1} from the value

Table 4. Thermal transport properties of the individual components of the reconstructed electrode coatings, electrode stacks, and cell stacks of cell A and cell B.

Material	Thermal conductivity [W m^{-1} K^{-1}]	Density [kg m^{-3}]	Heat capacity [J kg^{-1} K^{-1}]
Graphite	139[73–75]	2260[a]	715[a]
LCO	3.5[66–71]	5028[a]	716[a]
Copper (Cu)	399[90]	8960[90]	385[90]
Aluminum (Al)	237[90]	2700[90]	855[90]
Binder PVDF (B)	0.20[78–80]	1809[a]	1114[a]
CB	24[81–83]	2260[a]	650[a]
BCB 40 wt% CB	0.51[b]	1924[a]	928[b]
LP30	0.18[65]	1286[65]	1648[65]
He	0.03–0.06[87–89]	0.164[89]	5193[89]

[a]Experimentally determined value; [b]Modeled with Hamilton and Crosser.[84]

of LCO mentioned earlier. A common anode AM is graphite. Buerschaper et al.[73] determined an average thermal conductivity of 139 W m^{-1} K^{-1} for graphite, which shows a very good agreement with the values of Sangrós et al.[74] and Ho et al.[75] Therefore, the literature value of Buerschaper et al.[73] was chosen as the input parameter. The AM of the anodes show a several orders higher thermal conductivity in comparison to the cathodes. In our previous contribution,[37] we show that the limitation of the heat transport is not caused by the thermal conductivity of the AM but by the conductivity of the BCB mixture and the electrolyte. Because of the explained aforementioned inhibitions, the difference between the effective thermal conductivity of the anodes and cathodes is quite smaller than the difference between the thermal conductivity of their AMs. Therefore, the deviation of about 0.7 W m^{-1} K^{-1} between the bulk thermal conductivity of the cell chemistry NMC and LCO for this investigation is negligible. The AMs of the KOKAM cells A and B consist of graphite for the anode coatings and a mixture of LCO/lithium-nickel-cobalt-aluminum-oxide (NCA) for the cathode coatings. As no literature values were available for NCA and the thermal conductivity of the cathode AM only has a minor influence, LCO was chosen as input parameter for AM of the cathode coatings.

The BCB phase is a heterogeneous system which will be approximated homogeneously for computational efficiency in our contribution. The images of the FIB–SEM tomography can be used to determine the fraction of the BCB mixture in the porous electrode coatings, but the ratio of the binder fraction to the carbon black (CB) fraction cannot be determined based on the images. The typical composition of the BCB phase of commercial electrodes varies between 50 and 70 wt% binder and 50 and 30 wt% CB, depending on the type of electrode.[52,76,77] Considering the literature values mentioned earlier, a simulation study was carried out by varying the CB fraction between 30 and 50 wt%. We limited the fraction in the BCB composite to an average value of 40 wt% as the effective thermal conductivities of the simulation results showed no significant dependency on the CB fraction. The commonly used polymer polyvinylidene-fluoride (PVDF), which has a thermal conductivity of about 0.2 W m^{-1} K^{-1}, was chosen for the binder phase.[78–80] The CB shows a significantly higher bulk thermal conductivity of 24 W m^{-1} K^{-1}.[81–83] The effective thermal conductivity of the BCB composite is calculated according to the adapted model of Hamilton and Crosser,[84] which we presented in detail in our previous publication.[37] This model results in an effective thermal conductivity of the BCB composite of 0.51 W m^{-1} K^{-1} for a CB fraction of 40 wt%.

A commonly used electrolyte is LP30, which consists of a mixture of dimethyl carbonate and ethylene carbonate. Werner et al.[65] determined the thermal conductivity of LP30 to be 0.18 W m^{-1} K^{-1}. The laser-flash analysis is used for the experimental determination of the effective thermal conductivity of porous electrode stacks in this work. The principle of the laser-flash analysis is explained in detail in the publication of Parker et al.[85] Maleki et al.,[7] and Gotcu et al.[86] applied the laser-flash analysis to porous electrode stacks in their contributions. The contributions mentioned are recommended for more detailed information. We chose helium instead of LP30 as the filling fluid for the pore space. This was because of the extremely

volatile electrolytes and their incompatibility with established measurement methods as well as the laser-flash analysis. Considering helium as the filling fluid, it is possible to validate our model approaches with experimental measurement data. Therefore, the thermal transport parameters of helium are initially used in our models for the validation of the simulation results. In a next step, the thermal transport properties are replaced with those of LP30 in our models to determine the effective thermal conductivity under operating conditions. The Smoluchowski effect[87,88] must be considered for gases like helium due to the small pore size of the electrode coatings. Considering the experimentally determined pore sizes of cell A and cell B, the thermal conductivity of helium is reduced to 0.03 and 0.06 W m^{-1} K^{-1}.[87–89] We used copper and aluminum with thermal conductivity values of 399 and 237 W m^{-1} K^{-1} for the current collectors of the anodes and cathodes, respectively.[90]

4.3. Simulation Results

In the following, the analytical and the numerical models are verified against each other and validated with the experimental data of the electrode stacks and cell stacks of both of the KOKAM cells. In a first study, we investigated the influence of the particle contact area between the current collector layer and the separator layer on the effective thermal conductivity of porous anode and cathode coatings. An exemplary porous structure is shown in Figure 10a. The area in red represents the particle contact area to the separator layer or current collector layer. In this study, the particle contact area between the current collector layers is kept constant at a ratio of 0.2, whereby the contact area ratio between the separator layer and the AM particles was varied between 0.03 and 0.55. The results of the effective thermal conductivity of the anode coatings (red) and cathode coatings (blue) can be seen in Figure 10b. As shown in Figure 10, the effective thermal conductivity of both coatings is independent of the contact area ratio. An average effective thermal conductivity for the anode coatings of 1.75 and 1.1 W m^{-1} K^{-1} for the cathode coatings results. The identical conclusion is also valid for the influence of the contact

area ratio between the AM and the current collector layer. Therefore, the influence of the particle contact areas on the adjacent layers can be neglected and need not be considered in the studies in the following sections.

In the second study, the validity of the analytical series connection of thermal resistors (see Equation (4) in Section 3.2) is checked against the numerical results for electrode stacks and cell stacks. Therefore, the steady-state temperature profile was evaluated for the generically reconstructed electrode stacks and cell stacks of both the KOKAM cells. The stationary temperature profile of the cell stack of cell A is shown exemplarily in **Figure 11**a. Figure 11b shows the dimensionless mean temperature along the heat conduction direction (z-axis) of infinitesimal volume segments. A mean linear temperature profile can be recognized in each of the individual layers of the composed cell stack. The current collectors show a low-temperature gradient over the layer thickness due to their high thermal conductivity, in contrast to the electrode and separator layers, which show a high-temperature gradient due to their low thermal conductivity. It is also evident that the separator layer represents the greatest thermal resistance. The linear temperature profile of the electrode coatings also indicate a homogenous distribution of the AM particles and the BCB distribution in the heat conduction direction. In summary, the average temperature profile of the cell stack is characteristic for a classical series connection of thermal resistors.

We used Equation (5) to calculate the thermal conductivity of the individual layers for the verification of this assumption. Here, $\overline{\Delta T}$ and $\overline{\dot{Q}}$ correspond to the mean temperature gradient and mean heat flow, L_i to the individual layer thickness, and A to the cross-sectional area of the cell stack.

$$\lambda_{\text{layer}} = \frac{\overline{\dot{Q}} \cdot L_i}{A \cdot \overline{\Delta T}} \tag{5}$$

Equation (6) represent the series connection of the thermal resistors of the individual cell stack layers, according to the Figure 11a.
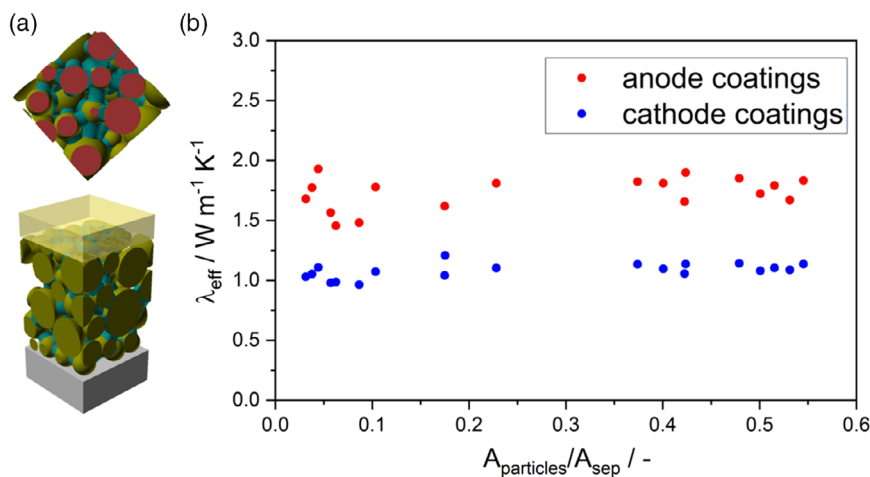
Figure 10. a) Illustration of an exemplary porous structure with particle contact areas in red. b) Illustration of the dependence of the effective thermal conductivity on the contact area ratio between the AM particles and the separator layer.
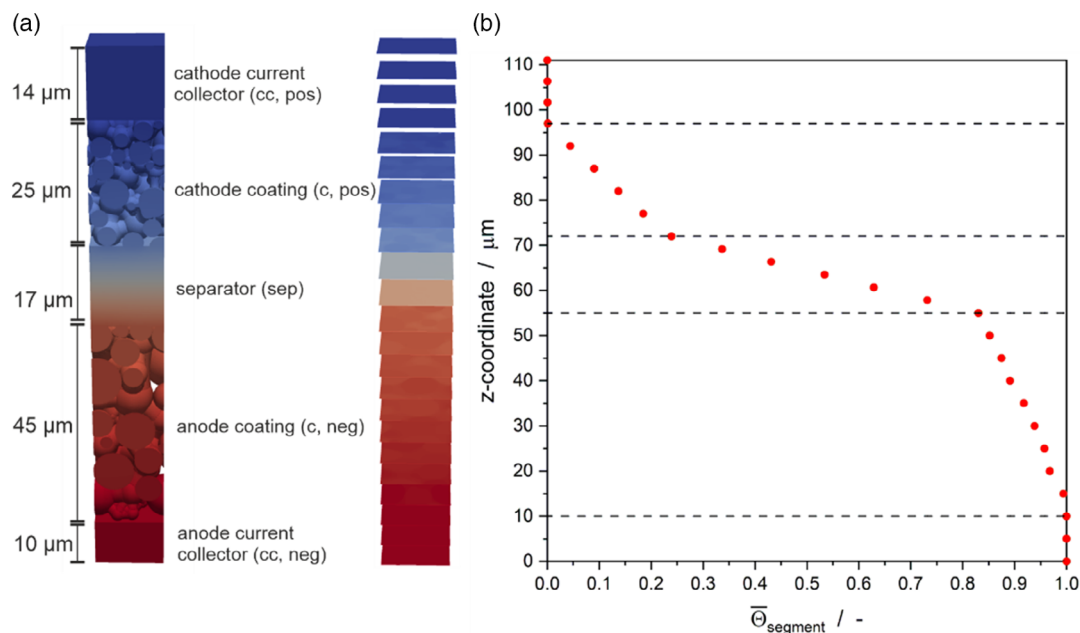
Figure 11. a) Representation of the temperature profile of the cell stack of cell A. b) Illustration of the stationary temperature profile along the heat conduction direction (z-axis) of volume segments.

$$\frac{L_{\text{cellstack}}}{\lambda_{\text{eff}}} = \frac{1}{2} \cdot \frac{L_{\text{cc, pos}}}{\lambda_{\text{cc,pos}}} + \frac{L_{\text{c,pos}}}{\lambda_{\text{c,pos}}} + \frac{L_{\text{sep}}}{\lambda_{\text{sep}}} + \frac{L_{\text{c,neg}}}{\lambda_{\text{c,neg}}} + \frac{1}{2} \cdot \frac{L_{\text{cc,neg}}}{\lambda_{\text{cc,neg}}} \tag{6}$$

The effective thermal conductivity of the cell stack can be calculated by combining Equation (5) and (6) using the mean temperature profile and thicknesses of the individual layers. The analytical series connection of the individual layers results in a value of 1.09 W m^{-1} K^{-1} for the effective thermal conductivity, which deviates by only 0.1% compared with the direct simulation of the entire cell stack. The effective thermal conductivity of the entire cell stack in the direct simulation is calculated via Equation (2), with the applied temperature gradient along the system limitations. The validity of the series connection is confirmed by the excellent agreement of the effective thermal conductivity with the value of the direct simulation. Therefore, to save computing time, only the porous electrode coatings must be simulated. Afterward, the effective thermal conductivity of the entire electrode stacks or cell stacks can be calculated using the thermal series connection of the individual cell layers according to Equation (5) and (6).

We compare the experimentally determined effective thermal conductivities of the electrode stacks for both KOKAM cells for the validation of the numerical and analytical model in the following. The results for the cathode stack of cell A are shown on the left-hand side and for the cathode stack of cell B on the right-hand side of **Figure 12**, depending on the filling fluid (helium and LP30). The red bars describe the effective thermal conductivity of the direct simulation of the entire electrode stack, whereas the blue bars describe the effective thermal conductivity calculated by a series connection of the individual thermal conductivities of the electrode layers, see Equation (4). The red bars show an excellent agreement with a maximal deviation of only

0.03% in comparison to the blue bars. As reported in Section 4.2, helium is initially used as the filling fluid for the validation of the numerical and analytical models and, in a next step, replaced by LP30 to determine the effective thermal conductivity under operating conditions.

An experimental value of 1.08 ± 0.09 W m^{-1} K^{-1} (green bar) was determined for the cathode stack of cell A with helium as the filling fluid, which deviates by only 1% from the simulation result, considering the experimental uncertainty and the stochasticity of the numerical results. The analytical model (violet bar) shows a maximal deviation of 11% to from the experimental results. The increase in the effective thermal conductivity of the direct simulation by replacing the filling fluid of helium with LP30 is about 33%. The numerical and analytical models deviate by only 12% for LP30 as the filling fluid.
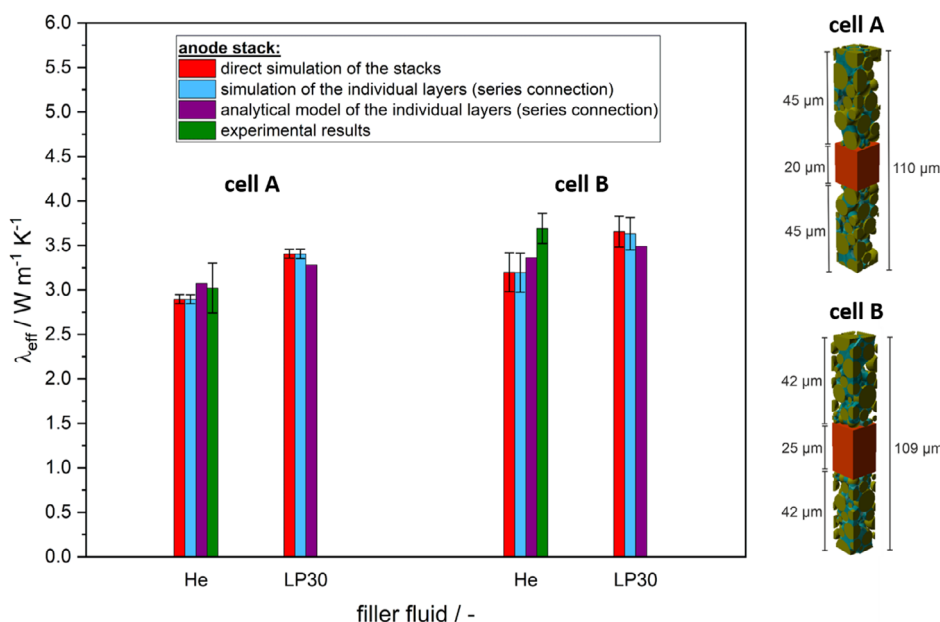
An experimental value of 1.42 ± 0.21 W m^{-1} K^{-1} (green bar) was determined for the cathode stack of cell B with helium as the filling fluid; the uncertainty of the experiment overlaps with the values of the simulation (red bar) and the analytical model (violet bar). The increase in the effective thermal conductivity of the direct simulation by replacing the helium filling fluid with LP30 is about 30%. The numerical and analytical models deviate by only 11% for LP30 as the filling fluid.

The results for the anode stack of cell A are shown on the left-hand side and cell B on the right-hand side in **Figure 13**, depending on the filling fluid (helium and LP30). The direct simulation (red bars) show an excellent agreement with a maximal deviation of only 0.03% compared with the series connection of the individual thermal conductivities of the electrode layers (blue bars).

An experimental value of 3.02 ± 0.28 W m^{-1} K^{-1} (green bar) was determined for the anode stack of cell A with helium as the filling fluid; the uncertainty of the experiment overlaps with the values of the simulation (red bar) and the analytical model (violet
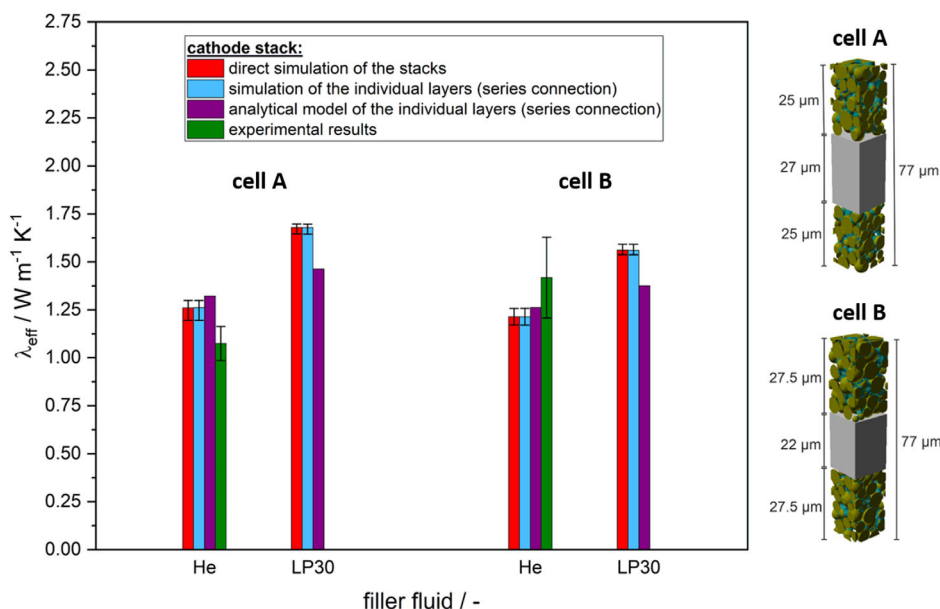
Figure 12. Comparison of the simulation results (red bars and blue bars) of the cathode stacks of cell A (left) and cell B (right) with the results of the analytical model (violet bars) and the corresponding measurement data (green bars).

Figure 13. Comparison of the simulation results (red bars and blue bars) of the anode stacks of cell A (left) and cell B (right) with the results of the analytical model (violet bars) and the corresponding measurement data (green bars).

bar). The increase in the effective thermal conductivity of the direct simulation by replacing the helium filling fluid with LP30 is about 18%. The numerical and analytical models deviate by only 3% for LP30 as the filling fluid.

An experimental value of $3.69 \pm 0.22 \, \mathrm{W \, m^{-1} \, K^{-1}}$ (green bar) was determined for the cathode stack of cell B with helium as the filling fluid, which deviates by only 2% from the simulation result (red bar), considering the experimental uncertainty and

the stochasticity of the numerical results. The analytical model (violet bar) shows a maximal deviation of 3% from the experimental results. The increase in the effective thermal conductivity of the direct simulation by replacing the helium filling fluid with LP30 is about 30%. The numerical and analytical models deviate by only 2% for LP30 as the filling fluid.

The experimental results in Figure 12 and 13 show for the filling fluid helium a significantly higher uncertainty compared

**ADVANCED
SCIENCE NEWS**

www.advancedsciencenews.com

Energy Technology
Generation, Conversion, Storage, Distribution

www.entechnol.de

with the numerical simulations. The uncertainty of the numerical simulations can be explained due to the varying morphology of the electrode structures caused by the structure generation process. As the thermal conductivity of the filling fluid helium is strongly reduced compared with the electrolyte LP30, see Table 4, the morphological inhomogeneities of the solid phase become more apparent and are reflected in a higher uncertainty of the effective thermal conductivity. For the experimental results, in addition to the uncertainties of the measurement method, the stochasticity of the electrode coatings of the stacks is included. Therefore, five different electrode stacks are measured three times per cell to regard the stochasticity of the electrode coatings in the uncertainty of the experimental results. Based on this, the experimental results show a significantly higher uncertainty compared with the numerical simulations and can vary for different cells and coatings in a wider range.

In the next studies, the effective thermal conductivity of both the KOKAM cell stacks perpendicular and parallel to the layers will be discussed. In a first step, we estimate the range of effective thermal conductivity of porous separator layers according to the models explained previously in Section 3.3, as no experimental measurement results were available. Therefore, research into the morphological parameters, material compositions, and their bulk material thermal conductivities was carried out. Typical porosities of commercial separators vary between 30 and 70 vol%, according to Abraham, Djian et al., and Patel et al.[91–93] The pore spaces of the porous separators are filled with electrolyte. The solid phase of separators usually consists of polyethylene and polypropylene. The bulk thermal conductivity of polyethylene varies between 0.3 and 0.44 W m^{-1} K^{-1}[63,64] and of polypropylene between 0.12 and 0.22 W m^{-1} K^{-1}.[62,63] We chose LP30 as the electrolyte for the fluid phase. Based on the parameter sets mentioned earlier, such as the porosity and the bulk thermal conductivities ranges, a variation of the effective thermal conductivities of the separator was carried out using the analytical models presented in Section 3.3. The bounds of the models are shown in **Table 5**. The models generally show a very good agreement in comparison with each other and with the experimental values of Richter et al.,[28] which also vary in a value range of 0.1–0.4 W m^{-1} K^{-1}.

Considering the analytically and experimentally determined values, the effective thermal conductivities of the separators λ_{sep} were varied in the following studies in a range of 0.1–0.4 W m^{-1} K^{-1}. **Table 6** shows the effective perpendicular thermal conductivities determined by the direct simulation,
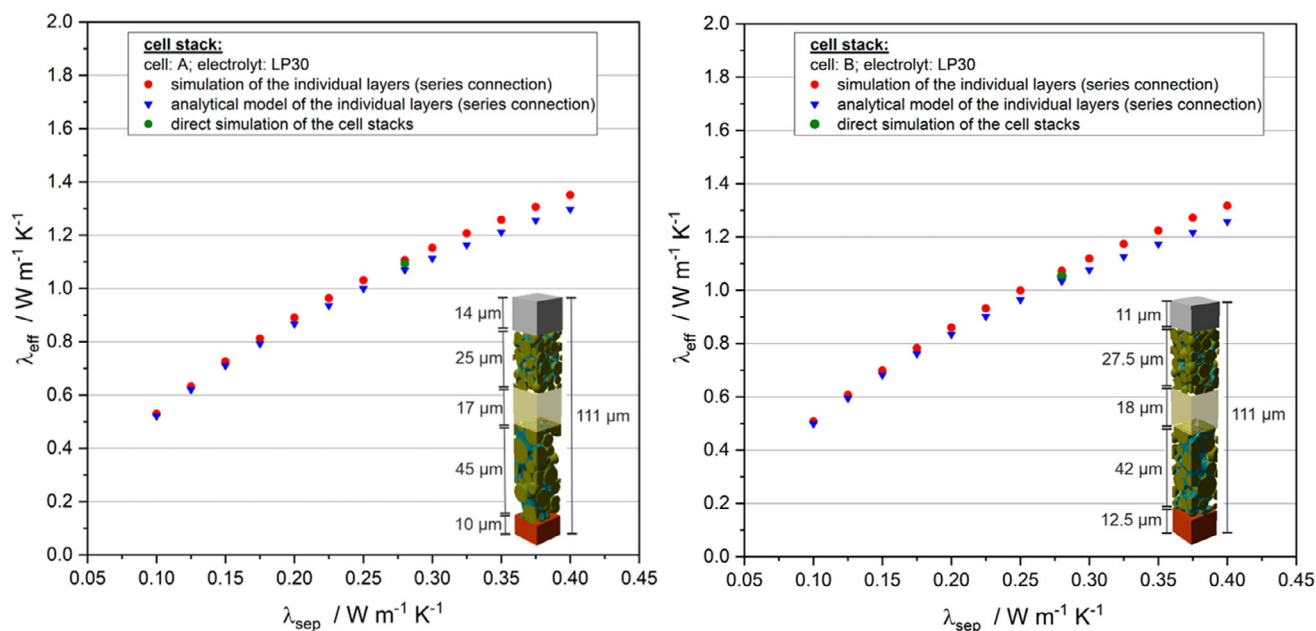
Table 6. Effective perpendicular thermal conductivity for both KOKAM cell stacks A and B, determined by the direct simulation, the series connection of the individually simulated cell layers and the analytical model for an input thermal conductivity of the separator layers of 0.28 W m^{-1} K^{-1}.

| Method	λ_{sep} [W m^{-1} K^{-1}]	$\lambda_{eff,stack}$ [W m^{-1} K^{-1}]	
		Cell A	Cell B
Direct simulation	0.28	1.09	1.05
Series connection (simulation)	0.28	1.11	1.06
Series connection (analytical model)	0.28	1.07	1.02

the series connection of the individually simulated cell layers and the analytical model for a thermal conductivity of the separator layers of 0.28 W m^{-1} K^{-1}. The latter value was estimated from the mean thermal conductivities of various separators experimentally determined by Richter et al.[28] The results of the direct simulation and the series connection of the individual simulated cell layers differ for both cell A and cell B by only 2%. The analytical model also shows a slight deviation of 4% compared with the direct simulation of the entire cell stack. No further direct simulations were carried out below due to the excellent agreement between the direct simulation and the series connection and a reduction in the computing time.

Figure 14 shows the effective perpendicular thermal conductivity of the cell stacks of cell A and cell B as a function of the separator thermal conductivity bounds estimated previously. The effective thermal conductivities for both cell stacks calculated by the simulative regarded series connection vary in a range of 0.5–1.35 W m^{-1} K^{-1}. The effective thermal conductivities determined by the analytical model result in values for both cell stacks between 0.5 and 1.25 W m^{-1} K^{-1}. The maximum deviation between the two models is only about 3%. The results presented are in an excellent agreement with typical literature values of different round, pouch, and prismatic cells,[31–36] which vary between 0.15 and 1.63 W m^{-1} K^{-1}. Considering the thermal resistances of the individual cell layers, the separator layer was identified as the limiting factor for the effective perpendicular thermal conductivity. There are only minor deviations on average between cell A and cell B of about 3.5%. Reason for the small differences are the very similar thicknesses of the separator layers and their limiting thermal resistances compared with the other cell layers.

As mentioned in Section 3.3, the series and parallel connections for heterogeneous systems represent the minimal and maximal bounds of the effective thermal conductivity. Therefore, we investigated a parallel connection of the individual cell layers to determine the maximal effective thermal conductivity of both cell stacks. **Figure 15** shows the effective parallel thermal conductivity of both cell stacks depending on the thermal conductivity of the separator layer. In addition, the thermal conductivities of the aluminum and copper current collectors were varied by ±10 and ±20%. The results of the analytical model are not shown in Figure 15, due to the slight deviations of less than 0.2% compared with the simulation results. A comparison of the effective parallel with the effective perpendicular thermal conductivity values of both cell stacks shows a 50–60 times higher thermal

Table 5. Estimation of the separator thermal conductivity bounds depending on the porosity and bulk thermal conductivities of the polymers used for different analytical models.

Model	Porosity [vol%]	$\lambda_{polymer}$ [W m^{-1} K^{-1}]	λ_{sep} [W m^{-1} K^{-1}]
Parallel connection			0.13–0.37
Maxwell–Eucken I			0.12–0.34
EMT model	30–70	0.1–0.45	0.12–0.35
Maxwell–Eucken II			0.12–0.36
Series connection			0.12–0.31

2000722 (13 of 16)

**ADVANCED
SCIENCE NEWS**

www.advancedsciencenews.com

Energy Technology
Generation, Conversion, Storage, Distribution

www.entechnol.de

Figure 14. Illustration of the effective perpendicular thermal conductivity of the cell stacks of cell A and cell B as a function of the separator thermal conductivity bounds estimated.
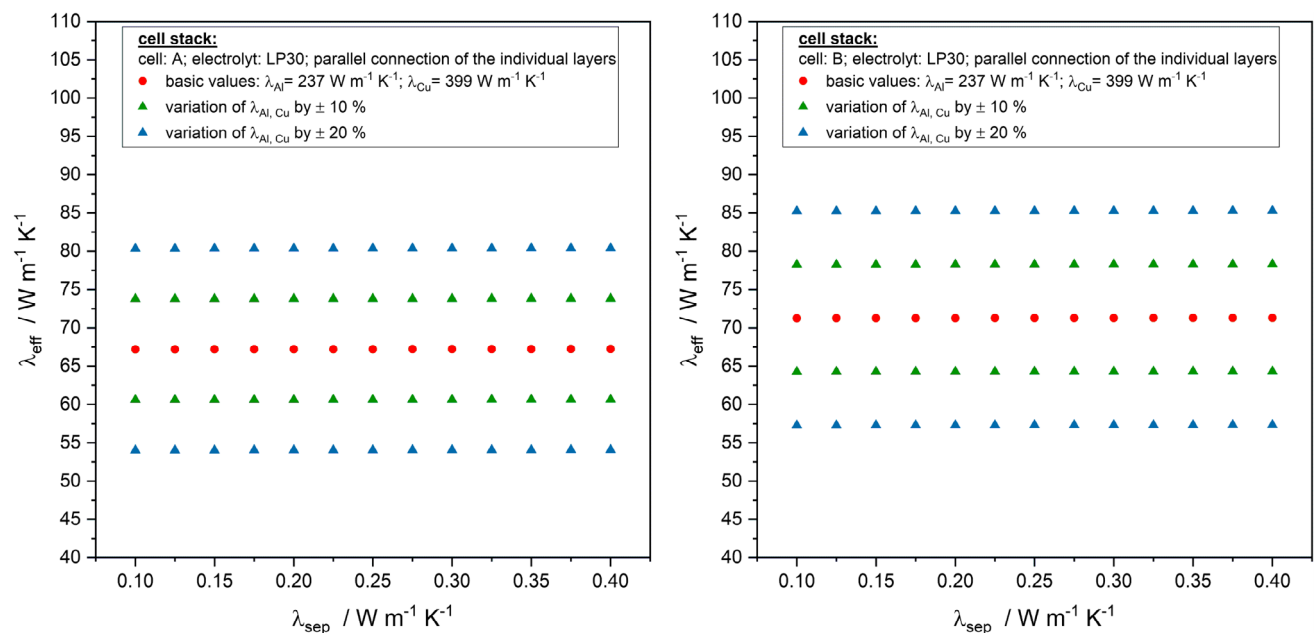
Figure 15. Illustration of the effective parallel thermal conductivity of the cell stacks of cell A and cell B as a function of the separator thermal conductivity bounds estimated and the thermal conductivity of the current collectors.

conductivity of the parallel connection of the layers (compare Figure 14 and 15). Figure 15 shows that the effective parallel thermal conductivity of the cell stack is independent of the thermal conductivity range of the separator layer considered. The variation of the thermal conductivities of the current collectors results in a directly proportional change of the effective thermal conductivities of the cell stacks by ±10 and ±20%.

5. Conclusion

In this work, a numerical and an analytical model for the effective thermal conductivity of porous electrode coatings were further developed to describe the according properties of electrode and cell stacks. The geometry of the porous electrode coatings, electrode stacks, and cell stacks of two commercial high-power

cells manufactured by KOKAM were reconstructed. Morphological parameter sets of the cells were taken from the study by Almar et al.[38] and unknown parameter sets were determined experimentally. In the first study, the influence of the particle contact areas on the current collector and separator layers was investigated. The study showed that the influence of the particle contact areas on the adjacent layers can be neglected and need not be considered. Based on this, we demonstrated the validity of the series connection of the thermal resistances of the individual cell layers compared with a direct simulation of the entire electrode or cell stacks.

A validation of the numerical and analytical model was carried out based on experimental measurement values of the reconstructed electrode stacks of the KOKAM cells. The effective thermal conductivities of the numerical model deviate by a maximum of 2% from the experimental values and 11% from the analytical model. The numerical and the analytical models show a maximum deviation of 12%.

Finally, effective thermal conductivities of both KOKAM cell stacks perpendicular and parallel to the layers were determined. First, the upper and lower thermal conductivity bounds of the separator were estimated with classic models for binary heterogeneous systems. Values between 0.1 and $0.4 \, \mathrm{W \, m^{-1} \, K^{-1}}$ were obtained, which correspond to the known literature values of Richter et al.[28] A range of 0.5–$1.35 \, \mathrm{W \, m^{-1} \, K^{-1}}$ for the effective perpendicular thermal conductivity of the cell stacks and a range of 66–$72 \, \mathrm{W \, m^{-1} \, K^{-1}}$ for the effective parallel thermal conductivity were determined. The values for the perpendicular thermal conductivity are in good agreement with common literature values of different round, pouch, and prismatic cells.[31–36] The heat transport in the considered LIB cells is limited mainly by the low thermal conductivity of the separator layers.

Conflict of Interest

The authors declare no conflict of interest.

[1] T. M. Bandhauer, S. Garimella, T. F. Fuller, *J. Electrochem. Soc.* **2011**, *158*, R1.
[2] J. Vetter, P. Novák, M. R. Wagner, C. Veit, K. C. Möller, J. O. Besenhard, M. Winter, M. Wohlfahrt-Mehrens, C. Vogler, A. Hammouche, *J. Power Sources* **2005**, *147*, 269.
[3] D. Werner, S. Paarmann, A. Wiebelt, T. Wetzel, *Batteries* **2020**, *6*, 12.
[4] D. Werner, S. Paarmann, A. Wiebelt, T. Wetzel, *Batteries* **2020**, *6*, 13.
[5] D. Bernardi, E. Pawlikowski, J. Newman, *J. Electrochem. Soc.* **1985**, *132*, 5.
[6] J. Newman, W. Tiedemann, *AIChE J.* **1975**, *21*, 25.
[7] H. Maleki, S. A. Hallaj, R. J. Selman, R. B. Dinwiddie, H. Wang, *J. Electrochem. Soc.* **1999**, *146*, 947.
[8] A. Loges, S. Herberger, P. Seegert, T. Wetzel, *J. Power Sources* **2016**, *336*, 341.
[9] J. P. Schmidt, *PhD Thesis*, Karlsruhe Institute of Technology (Karlsruhe, Germany) **2003**.
[10] M. G. Zeyen, A. Wiebelt, in *Handbuch Lithium-Ionen-Batterien* (Ed: R. Korthauer), Springer Vieweg, Berlin Heidelberg, Germany **2013**.
[11] R. W. Atkinson, R. Carter, C. T. Love, *Energy Storage Mater.* **2019**, *22*, 18.
[12] R. Carter, C. T. Love, *ACS Appl. Mater. Interfaces* **2018**, *10*, 26328.
[13] M. Petzl, *PhD Thesis*, Ulm University (Ulm, Germany) **2015**.
[14] T. Waldmann, M. Wilka, M. Kasper, M. Fleischhammer, M. Wohlfahrt-Mehrens, *J. Power Sources* **2014**, *262*, 129.
[15] A. Jossen, W. Weydanz, *Moderne Akkumulatoren Richtig Einsetzen*, 2nd ed., Cuvillier Verlag, Göttingen, Germany **2019**.
[16] S. F. Schuster, T. Bach, E. Fleder, J. Müller, M. Brand, G. Sextl, A. Jossen, *J. Energy Storage* **2015**, *1*, 44.
[17] P. Ramadass, B. Haran, R. White, B. N. Popov, *J. Power Sources* **2002**, *112*, 606.
[18] P. Ramadass, B. Haran, R. White, B. N. Popov, *J. Power Sources* **2002**, *112*, 614.
[19] G. Zhang, S. Huang, G. J. Nelson, T. Iriyama, G. M. Cavalheiro, *J. Electrochem. Energy Convers. Storage* **2020**, *17*, 1.
[20] F. Fleckenstein, O. Bohlen, B. Bäker, *World Electr. Veh. J* **2012**, *5*, 322.
[21] G. Guo, B. Long, B. Cheng, S. Zhou, P. Xu, B. Cao, *J. Power Sources* **2010**, *195*, 2393.
[22] D. H. Jeon, S. M. Baek, *Energy Convers. Manage.* **2011**, *52*, 2973.
[23] F. Yue, G. Zhang, J. Zhang, J. Lin, K. Jiao, *Appl. Therm. Eng.* **2017**, *126*, 70.
[24] M. Chen, F. Bai, W. Song, J. Lv, S. Lin, Z. Feng, Y. Li, Y. Ding, *Appl. Therm. Eng.* **2017**, *120*, 506.
[25] A. Samba, N. Omar, H. Gualous, O. Capron, P. Van den Bossche, J. Van Mierlo, *Electrochim. Acta* **2014**, *147*, 319.
[26] A. Samba, N. Omar, H. Gualous, Y. Firouz, P. Van den Bossche, J. Van Mierlo, T. I. Boubekeur, *Electrochim. Acta* **2014**, *117*, 246.
[27] S. Goutam, A. Nikolian, J. Jaguemont, J. Smekens, N. Omar, P. Van Dan Bossche, J. Van Mierlo, *Appl. Therm. Eng.* **2017**, *126*, 796.
[28] F. Richter, S. Kjelstrup, P. J. S. Vie, O. S. Burheim, *J. Power Sources* **2017**, *359*, 592.
[29] A. Loges, S. Herberger, D. Werner, T. Wetzel, *J. Power Sources* **2016**, *325*, 104.
[30] S. C. Chen, C. C. Wan, Y. Y. Wang, *J. Power Sources* **2005**, *140*, 111.
[31] S. J. Drake, D. A. Wetz, J. K. Ostanek, S. P. Miller, J. M. Heinzel, A. Jain, *J. Power Sources* **2014**, *252*, 298.
[32] K. A. Murashko, A. V. Mityakov, J. Pyrhönen, V. Y. Mityakov, S. S. Sapozhnikov, *J. Power Sources* **2014**, *271*, 48.
[33] S. J. Bazinski, X. Wang, *J. Power Sources* **2015**, *293*, 283.
[34] L. Sheng, L. Su, H. Zhang, *Int. J. Heat Mass Transf.* **2019**, *139*, 231.
[35] J. Zhang, B. Wu, Z. Li, J. Huang, *J. Power Sources* **2014**, *259*, 106.
[36] H. Maleki, H. Wang, W. Porter, J. Hallmark, *J. Power Sources* **2014**, *263*, 223.

[37] D. Oehler, P. Seegert, T. Wetzel, *Energy Technol.* **2020**, 2000574.

[38] L. Almar, J. Joos, A. Weber, E. Ivers-Tiffée, *J. Power Sources* **2019**, *427*, 1.

[39] E. G. Gilbert, D. W. Johnson, S. S. Keerthi, *IEEE J. Robot. Autom.* **1988**, *4*, 193.

[40] P. von Böckh, T. Wetzel, *Wärmeübertragung Grundlagen und Praxis*, 7th ed., Springer Vieweg, Berlin, Germany **2017**.

[41] P. Zehner, E. U. Schlünder, *Chem. Ing. Technol.* **1970**, *14*, 933.

[42] P. Zehner, E. U. Schlünder, *Chem. Ing. Technol.* **1972**, *23*, 1303.

[43] P. Zehner, E. U. Schlünder, *Chem. Ing. Technol.* **1973**, *5*, 272.

[44] J. Lee, C.-L. Lee, K. Park, I.-D. Kim, *J. Power Sources* **2014**, *248*, 1211.

[45] J.-L. Shi, L.-F. Fang, H. Li, H. Zhang, B.-K. Zhu, L.-P. Zhu, *J. Membr. Sci.* **2013**, *437*, 160.

[46] Z. Hashin, S. Shtrikman, *J. Appl. Phys.* **1962**, *33*, 3125.

[47] A. Eucken, *Forschungsarb. Gebiete Ingenieurw.* **1940**, *11*, 6.

[48] J. K. Carson, S. J. Lovatt, D. J. Tanner, A. C. Cleland, *Int. J. Heat Mass Transf.* **2005**, *48*, 2150.

[49] S. Kirkpatrick, *Rev. Mod. Phys.* **1973**, *45*, 574.

[50] R. Landauer, *J. Appl. Phys.* **1952**, *23*, 779.

[51] N. C. Gallego, C. I. Contescu, H. M. Meyer, J. Y. Howe, R. A. Meisner, E. A. Payzant, M. J. Lance, S. Y. Yoon, M. Denlinger, D. L. Wood, *Carbon* **2014**, *72*, 393.

[52] L. Pfaffmann, C. Birkenmaier, M. Müller, W. Bauer, T. Mitsch, J. Feinauer, Y. Krämer, F. Scheiba, A. Hintennach, T. Schleid, V. Schmidt, H. Ehrenberg, *J. Power Sources* **2016**, *307*, 762.

[53] K. Zaghib, X. Song, A. Guerfi, R. Rioux, K. Kinoshita, *J. Power Sources* **2003**, *119–121*, 8.

[54] M. Indrikova, S. Grunwald, F. Golks, A. Netz, B. Westphal, A. Kwade, *J. Electrochem. Soc.* **2015**, *162*, A2021.

[55] W. Bauer, D. Nötzel, V. Wenzel, H. Nirschl, *J. Power Sources* **2015**, *288*, 359.

[56] L. Pfaffmann, S. Jaiser, M. Müller, P. Scharfer, W. Schabel, W. Bauer, F. Scheiba, H. Ehrenberg, *J. Power Sources* **2017**, *363*, 460.

[57] H. Wang, T. Umeno, K. Mizuma, M. Yoshio, *J. Power Sources* **2008**, *175*, 886.

[58] M. Yoo, C. W. Frank, S. Mori, *Chem. Mater.* **2003**, *15*, 850.

[59] S. Carelli, M. Quarti, M. C. Yagci, W. G. Bessler, *J. Electrochem. Soc.* **2019**, *166*, A2990.

[60] S. Gantenbein, M. Weiss, E. Ivers-Tiffée, *J. Power Sources* **2018**, *379*, 317.

[61] M. Mayur, M. C. Yagci, S. Carelli, P. Margulies, D. Velten, W. G. Bessler, *Phys. Chem. Chem. Phys.* **2019**, *21*, 23672.

[62] L. Chen, H. F. Xu, S. J. He, Y. H. Du, N. J. Yu, X. Z. Du, J. Lin, S. Nazarenko, *PLoS One* **2017**, *12*, 0170523.

[63] I. L. Ngo, C. Byon, in *Polymer Science: Research Advances, Partical Applications and Educational Aspects*, (Eds: A. Mendez-Vilas, A. Solano), **2016**.

[64] C.-M. Ye, B.-Q. Shentu, Z.-X. Weng, *J. Appl. Polym. Sci.* **2006**, *101*, 3806.

[65] D. Werner, A. Loges, D. J. Becker, T. Wetzel, *J. Power Sources* **2017**, *364*, 72.

[66] J. Cho, M. D. Losego, H. G. Zhang, H. Kim, J. Zuo, I. Petrov, D. G. Cahill, P. V. Braun, *Nat. Commun.* **2014**, *5*, 4035.

[67] T. Feng, A. O'Hara, S. T. Pantelides, *Nano Energy* **2020**, *75*, 104916.

[68] J. He, L. Zhang, L. Liu, *Phys. Chem. Chem. Phys.* **2019**, *21*, 12192.

[69] S. Mizuno, H. Fujishiro, M. Ishizawa, T. Naito, H. Katsui, T. Goto, *Jpn. J. Appl. Phys.* **2017**, *56*, 021101.

[70] K. Takahata, I. Terasaki, *Jpn. J. Appl. Phys.* **2002**, *41*, 763.

[71] H. Yang, J. Y. Yang, C. N. Savory, J. M. Skelton, B. J. Morgan, D. O. Scanlon, A. Walsh, *J. Phys. Chem. Lett.* **2019**, *10*, 5552.

[72] E. J. Cheng, K. Hong, N. J. Taylor, H. Choe, J. Wolfenstine, J. Sakamoto, *J. Eur. Ceram. Soc.* **2017**, *37*, 3213.

[73] R. A. Buerschaper, *J. Appl. Phys.* **1944**, *15*, 452.

[74] C. Sangrós, C. Schilde, A. Kwade, *Energy Technol.* **2016**, *4*, 1611.

[75] C. Y. Ho, R. W. Powell, P. E. Liley, *J. Phys. Chem. Ref. Data* **1972**, *1*, 279.

[76] S. Jaiser, M. Müller, M. Baunach, W. Bauer, P. Scharfer, W. Schabel, *J. Power Sources* **2016**, *318*, 210.

[77] C. Meyer, H. Bockholt, W. Haselrieder, A. Kwade, *J. Mater. Process. Technol.* **2017**, *249*, 172.

[78] B. Bonno, J. L. Laporte, R. Tascón d'León, *Meas. Sci. Technol.* **2001**, *12*, 671.

[79] G. Krishna Bama, P. Indra Devi, K. Ramachandran, *J. Mater. Sci.* **2009**, *44*, 1302.

[80] Solvey, Solef PVDF Technical Data Sheets, https://www.solvay.com/en/brands/solef-pvdf/technical-data-sheets (accessed: May 2020).

[81] R. I. Corp, Carbon Black, https://www.reade.com/products/carbon-black (accessed: May 2020).

[82] Y. He, H. T. Li, L.-X. Ma, *Adv. Mat. Res.* **2009**, *87–88*, 86.

[83] Y.-J. Kim, Y.-F. Tan, S. Kim, *J. Compos. Mater.* **2017**, *52*, 2047.

[84] R. L. Hamilton, O. K. Crosser, *Ind. Eng. Chem. Fundam.* **1962**, *1*, 187.

[85] W. J. Parker, R. J. Jenkins, C. P. Butler, G. L. Abbott, *J. Appl. Phys.* **1961**, *32*, 1679.

[86] P. Gotcu, W. Pfleging, P. Smyrek, H. J. Seifert, *Phys. Chem. Chem. Phys.* **2017**, *19*, 11920.

[87] H. Reiss, in *VDI-Wärmeatlas* (Ed: VDI-Gesellschaft), Springer-Verlag, Heidelberg, Germany **2013**.

[88] E. Tsotsas, in *VDI-Wärmeatlas* (Ed: VDI-Gesellschaft), Springer-Verlag, Heidelberg, Germany **2013**.

[89] M. Kleiber, R. Joh, in *VDI-Wärmeatlas* (Ed: VDI-Gesellschaft), Springer-Verlag, Heidelberg, Germany **2013**.

[90] C. Ullrich, C. Bodmer, in *VDI-Wärmeatlas* (Ed: VDI-Gesellschaft), Springer-Verlag, Heidelberg, Germany **2013**.

[91] K. M. Abraham, *Electrochim. Acta* **1993**, *38*, 1233.

[92] D. Djian, F. Alloin, S. Martinet, H. Lignier, J. Y. Sanchez, *J. Power Sources* **2007**, *172*, 416.

[93] K. K. Patel, J. M. Paulsen, J. Desilvestro, *J. Power Sources* **2003**, *122*, 144.